Volume 1 | Number 1 | Jan 2013 | Pages 1–100

Journal of
Materials Chemistry A

Materials for energy and sustainability
www.rsc.org/materialsA

Li⁺

ROYAL SOCIETY
OF CHEMISTRY

ROYAL SOCIETY
OF **CHEMISTRY**

www.rsc.org/materialsA

1   ***Beyond Graphene Foam, a New Form of Three-Dimensional Graphene for***
2   ***Supercapacitor Electrode***
3

4   *Lu Zhang [a], Derek DeArmond [a,b], Noe T. Alvarez [b] Daoli Zhao [c], Tingting Wang [c],*
5   *Guangfeng Hou [a], Rachit Malik [a], William R. Heineman [c], Vesselin Shanov [a,b] [*]*
6
7
8   [a] Department of Mechanical and Materials Engineering, University of Cincinnati,
9   Cincinnati, OH, 45221-0072, USA
10   [b] Department of Biomedical, Chemical and Environmental Engineering, University of
11   Cincinnati, OH, 45221-0012, USA
12   [c] Department of Chemistry, University of Cincinnati, Cincinnati, OH, 45221-0172, USA
13
14

15 **Abstract**

16

17   Graphene foam (GF) is a three-dimensional (3D) graphene structure that has been

18 intensively studied as electrode materials for energy storage applications. The porous

19 structure and seamlessly connected graphene flakes made GF a promising electrode

20 material for supercapacitors and batteries. However, the electrical conductivity of GF is

21 still unsatisfactory due to the lack of macropore size (~300 μm) control that hinders its

22 applications. Previously we reported a new seamless 3D graphene structure - graphene

23 pellet (GP) - with well-controlled mesopore size (~2 nm), high electrical conductivity

24 (148 S/cm) and good electromechanical properties that differ substantially from the

25 known GF. Here we demonstrated that the obtained 3D graphene structure is an ideal

26 scaffold electrode for pseudocapacitive materials and redox additive electrolyte system.

27 For example, after electrochemical coating with MnO_2, the GP/MnO_2 electrode shows

28 specific and volumetric capacitance up to 395 F g^{-1} and 230 F cm^{-3} at 1 A/g, respectively.

29 When combined with hydroquinone and benzoquinone redox additive electrolyte, the GP

30 shows a specific capacitance of 7813 F/g at 10 A/g. Moreover, when a GP/MnO_2

31 electrode was assembled with a GP/polypyrrole electrode, the obtained full cell showed

1   good electrochemical performance with a maximum energy density of 26.7 Wh/kg and a

2   maximum power density of 32.7 kW/kg, and a reasonable cycle life for practical

3   application. The ease in materials processing combined with the excellent electrical and

4   electromechanical properties make GP promising for a variety of energy storage

5   applications.

6

7   **1. Introduction**

8

9   The seamless three-dimensional (3D) graphene structure known as graphene foam

10   (GF), has attracted attentions due to partly inheriting the properties of two dimensional

11   (2D) graphene into its 3D structure [1]. GF morphology ensures a fast electron transfer on

12   the 3D graphene skeleton and its porous structure contributes to a high specific surface

13   area of this material. Therefore, since reported in 2011, GF has been intensively

14   investigated for application in energy storage due to its attractive properties, as described

15   below [2-11]. Dong et al reported a GF/MnO_2 composite prepared from $KMnO_4$ with a

16   specific capacitance of 560 F/g at 0.2 A/g in 1.0 M Na_2SO_4 [5]. Cao et al have introduced

17   GF with NiO coating and achieved a specific capacitance of 816 F/g at 5 mV/s in 3M

18   KOH [7]. GF was also employed as an electrode for redox additives electrolyte systems.

19   Luo et al tested GF/Ni foam/$Co(OH)_2$ composite in 0.08M $K_3Fe(CN)_6$/1M KOH

20   electrolyte and obtained a specific capacitance of 7514 F/g at 16 A/g. In this case only the

21   mass of $Co(OH)_2$ was used for the capacitance calculation [8].

22

23   Despite the unique structure of GF that contributes to a fast electron transfer on

24   graphene skeleton, this material exhibits a poor electrical conductivity of ~ 1 S/cm. As a

1 consequence, the electrical performance of pseudocapacitive materials such as MnO_2 and

2 polyaniline used in combination with GF for supercapacitors is not satisfactory. In

3 addition, the relatively slow chemical reactions in battery systems further limit the

4 application of GF in energy storage. The low electrical conductivity of GF is a result of

5 its porous structure. The large macropores help increasing the surface area of GF.

6 However, they also contribute a longer electron-transfer pathway that results in in a low

7 electrical conductivity. Another consequence of the GF morphology is reduction of its

8 mechanical strength. Because of this mechanical weakness the fabricated electrodes

9 require additional metal support of the current collectors in a supercapacitor arrangement.

10 The unfavorable porous structure of GF is inherited from its catalyst used in the

11 chemical vapor deposition (CVD) process called nickel foam (NF). NF is an expensive

12 material to synthesize graphene through CVD. Further, GF made from NF yields only 0.4

13 mg graphene per gram of Ni catalyst. This is a major hurdle that hinders the

14 manufacturing scale up of GF, making it not feasible for mass production of electrode

15 material. These drawbacks motivated researchers to work on improving the electrical

16 properties of 3D graphene without increasing the cost of its preparation. Graphene oxide

17 (GO) shows advantages in fabrication considering its low cost thus making it attractive as

18 electrode material in combination with pseudocapacitive materials such as MnO_2 [12-14].

19 However, even after a performed chemical reduction, the residual functional groups such

20 as carboxyl, carbonyl and hydroxyl in GO still decrease its electrical conductivity.

21 Moreover, restacking of graphene sheets during processing of GO into an electrode

22 decreases the specific surface area (SSA) of the overall electrode structure [7, 15-18]. The

23 ability of GO electrode to compensate the low electron transfer in pseudocapacitive

3

1   materials and accelerate the chemical processes in battery materials is also challenging

2   and not straightforward.

3   CVD made graphene usually exhibits probably the best materials quality in terms of

4   low defect concentration and high purity. Having in mind the drawbacks of NF as a

5   catalyst, other catalyst materials, such as nickel chloride and nickel powders, have been

6   studied recently to synthesize high quality 3D graphene through CVD [19-22]. The challenge

7   using this approach is to successfully consolidate the Ni-containing particles into a

8   sintered body that is capable to act as an efficient and inexpensive catalyst in the CVD

9   environment yielding 3D graphene with good electrical and mechanical properties.

10   Previously we reported making a seamless 3D graphene structure called graphene

11 pellet (GP) synthesized through CVD by processing inexpensive nickel powders as a

12 catalyst [19]. In this work our efforts have been expanded to demonstrate that the GP can

13 be successfully employed as an important new platform for fabricating high performance

14 electrode materials for energy storage applications.

15
16
17 **2. Experimental**
18
19 **2.1. Sample preparation**

20 *2.1.1. Fabrication of graphene pellet (GP)*

21   Nickel powder (Alfa Aesar) of 2~3 µm average particle size and 0.68 m^2 g^{-1} in

22 SSA was pelletized into a 6.4 cm diameter pellet using a hydraulic press (Carver,

23 973214A). The sample described above was heated up to 1000 °C in a tube furnace

24 (FirstNano, ET1000) under Ar (1000 sccm). Hydrogen (325 sccm) was then introduced

25 for 5 min, to reduce any metal catalyst oxide. Then, 25 sccm of CH_4 was introduced for 1

1 minute. The sample was then cooled to room temperature at a rate of ~100 °C min^{-1}

2 under Ar (1000 sccm) and H$_2$ (325 sccm). The final 3D graphene structure in the form of

3 pellet was produced by etching out nickel from the graphene/nickel pellet with 3M HCl

4 at 80 °C for 10 h. The obtained GP was washed with DI water to remove residual acid.

5 Details of the synthesis and fabrication of the GP procedures can be found elsewhere [19].

6

7 *2.1.2 Fabrication of GP/MnO$_2$ electrode*

8   MnO$_2$ was coated on the GP by electrodeposition in the following way. GP was

9 immersed into a plating solution containing 20 mM MnSO$_4$ and 100 mM Na$_2$SO$_4$, and

10 subjected to 5 min to 80 min deposition under constant current density of 2 mA/cm^2.

11 After electrodeposition, the GP was washed with DI water to remove residual electrolyte,

12 and then dried at 60 °C for 2 h. The mass of the sample was measured before and after

13 electrodeposition of MnO$_2$, using a microbalance (Sartorius Micro Balance MSE6.6S-

14 000-DF). This enabled the mass ratio of MnO$_2$ in the GP/MnO$_2$ composite to be

15 calculated.

16

17 *2.1.3 Fabrication of GP/polypyrrole (Ppy) electrode*

18   GP/Ppy hybrid electrode was synthesized using an in-situ polymerization method

19 [14]. Generally, a GP was immersed into a mixture solution of pyrrole (1000 µL, from

20 Sigma-Aldrich), ethanol/DI water/1 M HCl (1:1:1, v/v/v) and amine *p*-toluene-sulfonate

21 (pTSNH$_4$, dopant, from Byk). Ammonium persulfate (APS, (NH$_4$)$_2$S$_2$O$_8$, oxidant, from

22 Fisher Scientific) was then added to the mixture solution and the chemical polymerization

1   was carried out at 0-5 °C for 30 min. The as-made GP/Ppy sample was then washed with

2   DI water and dried at 50 °C.

3

4   *2.1.4 Assembly of GP/MnO₂ - GP/Ppy asymmetric ECs*

5   The asymmetric ECs were fabricated by making GP/MnO_2 composite as the positive

6   electrode, GP/Ppy composite as the negative electrode, and finally assembling both

7   electrodes into a coin cell device. The two electrodes were separated by an aqueous

8   electrolyte (1 M Na_2SO_4) soaked separator (nitrocellulose film).

9   **2.2. Analysis**

10   *2.2.1. Microscopic characterization*

11   Scanning electron microscopy (SEM) (FEI XL30, 15 kV) and Raman spectroscopy

12   (Renishaw inVia, excited by a 514 nm He–Ne laser with a laser spot size of $\sim$1 μm^2)

13   were used to characterize the GP. X-ray photoelectron spectroscopy (XPS) data were

14   obtained using a Phi 5300 X-ray Photoelectron Spectrometer with Mg K-alpha X-rays at

15   an accelerating voltage of 15.0 kV (hν = 1253.6 eV) in a chamber maintained at 10^{-9} Torr.

16   The high-resolution scans of C and low-resolution survey scans were analyzed for each

17   sample at two or more separate locations.

18

19   *2.2.2. Surface area and pore size measurement*

20   Brunauer-Emmett-Teller (BET) study of GPs. Nitrogen adsorption–desorption

21   isotherm and Barrett-Joyner-Halenda (BJH) pore size distribution were studied by using a

22   surface characterization analyzer (Micromeritics, 3Flex).

23

1   *2.2.3. Electrical and mechanical measurements*

2   A four-point probe device (Jandel RM3000) was used for electrical measurement

3   of the samples. For conducting the resistance retention test, a two-point probe device was

4   constructed and made. In this arrangement, copper wires were embedded and connected

5   to GP with silver paste, which enabled a reliable electrical contact between the copper

6   wires and the GP. A minimum of three samples was measured to calculate each error bar.

7

8   *2.2.4. Electrochemical measurements*

9   The electrochemical measurements were carried out with a Gamry instrument

10   (Interface 1000) at room temperature using three-electrode configuration for the GP and

11   GP/MnO$_2$ electrodes and two-electrode configuration for asymmetric ECs. In the three-

12   electrode configuration, the freestanding GP and GP/MnO$_2$ samples served as the

13   working electrode without the use of any metal support. They were combined with a

14   Ag/AgCl reference electrode and a Pt counter electrode in an electrolyte solution of 1 M

15   Na$_2$SO$_4$. Additives such as 50 mM hydroquinone (HQ) and 50 mM benzoquinone (BQ)

16   were prepared along with 1M H$_2$SO$_4$ and 30% acetic acid (stabilizer for HQ and BQ)

17   used as electrolyte. The electrochemical characteristics of ~0.2 mg GP, ~1 mg GP/MnO$_2$

18   composites (total mass of electrode with both GP and MnO$_2$) and ~5 mg asymmetric ECs

19   (total mass of two electrodes with both GP and active materials including Ppy and MnO$_2$)

20   were   evaluated   by   cyclic   voltammetry,   galvanostatic   charge-discharge   and

21   electrochemical impedance spectroscopy measurements over a frequency range from 10^5

22   to 10^{-2} Hz at a sinusoidal voltage amplitude of 10 mV.

1   The specific capacitance in the three-electrode system was calculated by using the

2   equation $C = It/(\Delta Vm)$, and the volumetric capacitance was calculated by a similar

3   expression $C_v = \rho C$, where I is the discharge current, t is the discharge time, ΔV is the

4   operating voltage window, m is the individual electrode mass (including GP and active

5   materials), and ρ is the density of the electrode[23].

6   To achieve good capacitance performance of the asymmetric electrochemical

7   supercapacitors (ECs), the mass of the two electrodes was balanced based on the

8   following equation: $C^-\Delta V^- m^- = C^+\Delta V^+ m^+$, where C is the specific capacitance of single

9   electrode, ΔV is the operating voltage window, and m is the mass of the electrode.

10   The energy density (E), power density (P) and maximal power density (P_m) were

11   calculated by the expressions: $E = C_{cell}(\Delta V)^2/2$, $P = E/t$, and $P_m = \Delta V^2/4Rm$, where C_{cell}

12   is the cell capacitance calculated by $C_{cell} = It/(\Delta Vm)$, ΔV is the operating voltage

13   window, t is the discharge time, I is the discharge current, m is the total mass of the two

14   electrodes, R is internal resistance calculated from IR drop of the charge-discharge curve

15   [24].

16

17   **3. Results and discussion**

18   In order to create a seamless CVD-made 3D graphene structure, a rational design of

19   a 3D structured catalyst is necessary to be in place. In our approach, nickel powder of 2

20   to 3 μm in diameter was pressed to form a nickel pellet and then sintered at 1000 °C

21   under protective gas flow of argon to prevent oxidation. The pressing and heating steps

22   enable sintering of the Ni powder through necking, which ultimately benefits the

23   formation of a continuous and interconnected three-dimensional graphene structure

1   during the sequential CVD [19]. GPs have a relatively low areal density of 4.5 g/m^2 as

2   shown in (**Fig.S1**. The process of sintering nickel particles is illustrated in **Figs.1a** and **b.**

3   The rough surface of nickel powder (**Fig.1a**) becomes smoother after sintering (**Fig.1b**)

4   which leads to formation of an interconnected structure. Right after sintering the Ni

5   powder in Ar, methane was introduced in the CVD reactor to synthesize graphene. The

6   latter was observed on the surface of the sintered nickel (**Fig.1c**). The freestanding GP

7   was obtained by etching out Ni using HCl acid (**Fig.1d**). **Fig.1e** shows SEM images of

8   GF and GP taken under the similar magnification. It is clearly recognizable that GF has a

9   much larger macropore size compared to GP. The highly porous structure of GF

10   contributes to a high surface area, but as the same time lowers its electrical conductivity

11   due to the prolonged electron pathway. As will be discussed later on, the electrical

12   conductivity of GF is by 2 orders lower compared to that of GP from this work.

13   Moreover, the used Ni catalyst in our study yields 3.0 mg graphene per gram of nickel

14   powder compared to the Ni foam yielding only 0.4 mg per gram of nickel (**Table 1**).

15   **Fig.1f** displays typical Raman spectra of a GP. Normally, fewer layers of graphene

16   were observed through Raman spectra after reducing the methane saturation time during

17   the CVD step. The obtained GP has robust mechanical properties resulting in a good

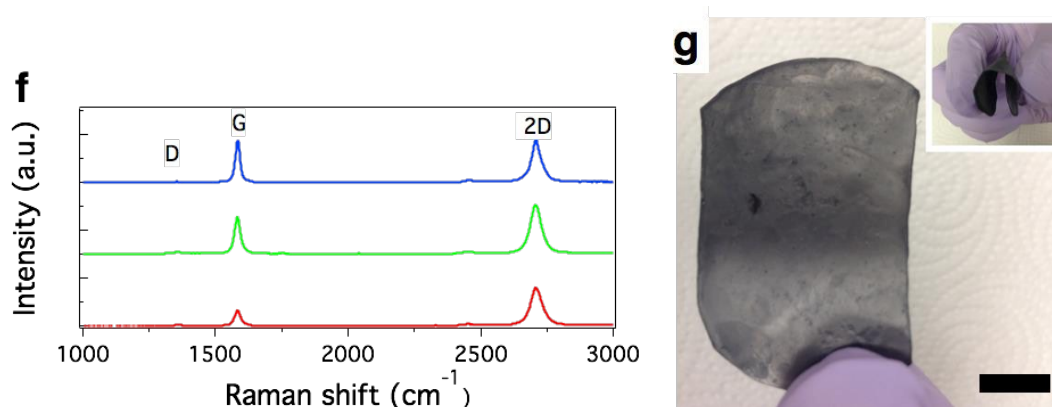18   flexibility, as illustrated in **Fig.1g**.
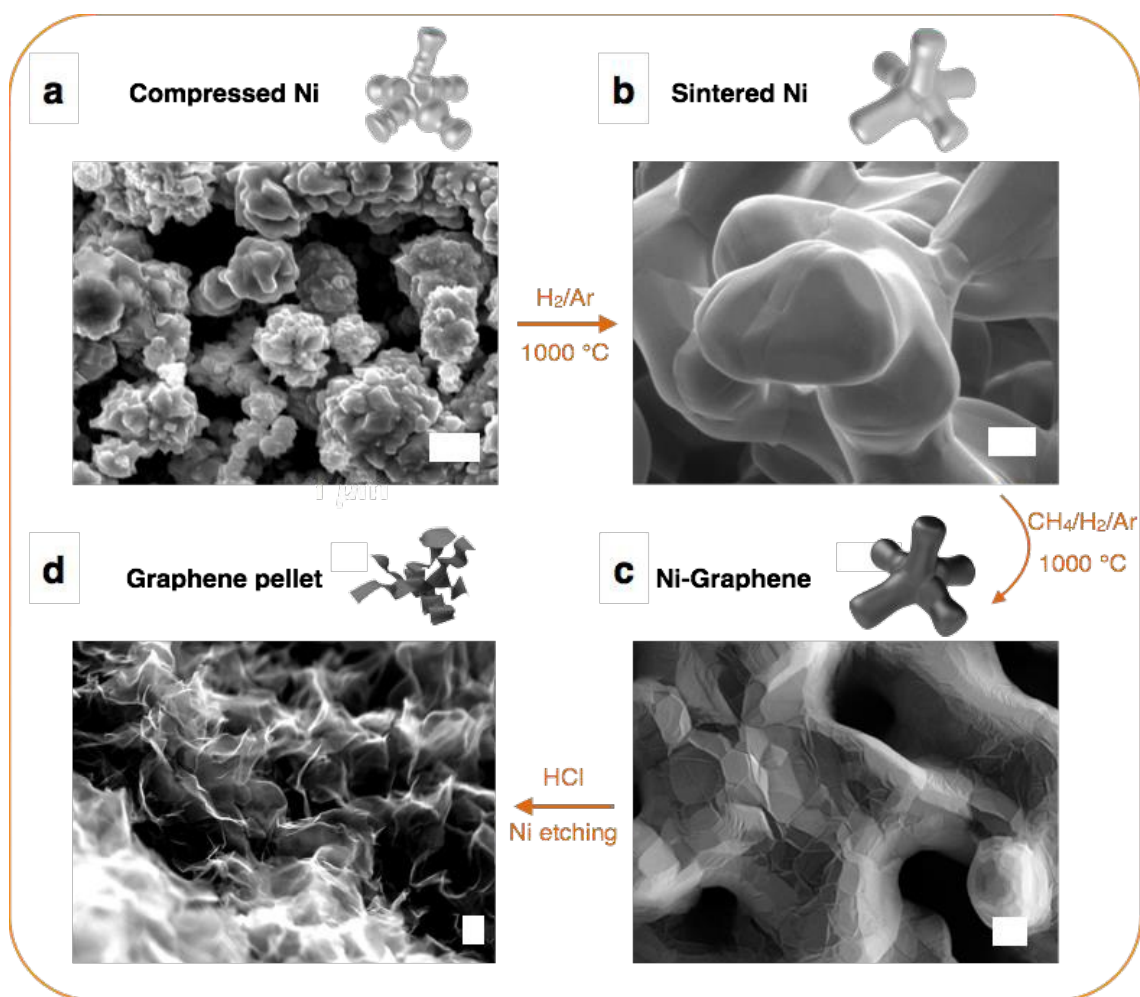
1
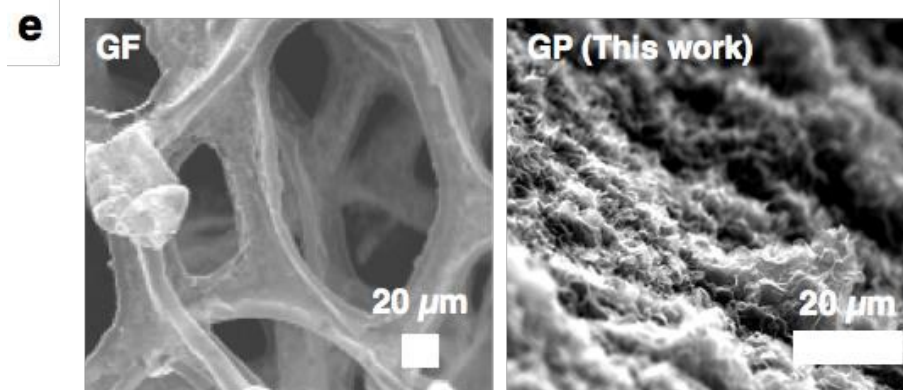
2

3

1

2 **Figure 1**. (a) Compressed Ni powder with discrete structure; (b) Sintered Ni powder with
3 continuous 3D structure; (c) CVD growth of 3D graphene structures on the sintered Ni
4 grains as a 3D scaffold template (Ni-Graphene); (d) Free-standing GP after etching the
5 sintered Ni with heated HCl acid. The scale bars correspond to 3 μm; (e) SEM images for
6 comparison of GF (left), and GP (right) (f) Typical Raman spectra of a GP prepared with
7 CH_4 concentration of 1.9 vol%. The three spectra suggest monolayer and multilayer
8 graphene (from bottom to top), respectively, which are examined based on the intensity,
9 shape and position of the G band and 2D band. (g) Photos of GP. The scale bar
10 corresponds to 1 cm. The inset shows good flexibility of GP.

11   **Table 2**. Comparison of graphene yielding and catalyst cost[*] for making GF and GP

Materials	Graphene yielding per gram of catalyst	Catalyst and cost
GF	0.4 mg	nickel foam ($0.6/g)
GP (this work)	3.0 mg	nickel powder ($0.15/g)

12   * Based on information from Thermo Fisher Scientific Inc.

13

14
15   The study of SSA, pore size distribution and electrical conductivity is important to

16   realize the performance of a carbon scaffold for pseudocapacitor application. Though the

17   obtained GP has a moderate SSA (~80 m^2/g), it shows a mesopore (~ 2 nm) dominated

18   structure (**Fig.S2**), which is beneficial in facilitating a quick diffusion of electrolyte ions

19   as suggested by other groups [25-27]. Furthermore, the electrical properties of GP are

1   outperforming other reported graphene scaffold materials for pseudocapacitor electrode

2   applications [1, 12, 28, 29] as shown in **Table 2**. The high electrical conductivity (148 S/cm) of

3   GP is attributed to the good quality of graphene prepared by CVD and improved flake to

4   flake contact compared to graphene samples obtained by wet chemistry methods [12, 29]. In

5   addition, due to the compression and the sintering process, the well interconnected nickel

6   grains helps to form a seamless 3D graphene structure, which results in a higher electrical

7   conductivity of the samples compared to other CVD made 3D graphene materials [1, 21, 28].

8   The electrical conductivity of the 3D graphene in this work can be controlled by the

9   methane concentration during the CVD process as demonstrated in **Fig. 2a.** It can be seen

10   there that the electrical conductivity of GP starts at a relative low value of 47 S/cm and

11   rises up to 148 S/cm with the increase of methane concentration during CVD. This

12   phenomenon could be attributed to the higher methane concentration causing more

13   graphene to grow on the sintered nickel skeleton, which results in a better-interconnected

14   graphene structure. It is worth mentioning that beyond a critical value of methane

15   concentration, the electrical conductivity decreases. This critical value in our work is 1.9

16   vol% as observed in **Fig.2a**. This is probably due to inability of the catalyst to absorb

17   methane when the methane concentration exceeds a certain saturating point [19].

18   The fast development of wearable devices and related power sources nowadays

19   demands for electrode materials with good mechanical and electrical properties [30]. GPs

20   have beneficial characteristics such as high electrical conductivity, good mechanical

21   robustness, and flexibility. Therefore, GPs are expected to perform well when

22   incorporated as flexible electrodes in devices integrated with woven and non-woven

23   fabric. We investigated the effect of bending on the electrical resistance of GPs prepared

1   by 1.9 vol% CH_4 with 1 min saturation time during CVD, which reveals the best

2   electrical conductivity among all the prepared samples. The bend and stretch tests were

3   carried out using a 4-point bending device and a high-precision mechanical system. The

4   electrical resistance revealed a small decrease when bending up to radius of 1.0 mm and

5   can recover after straightening with a resistance increase of only 0.21 % (**Fig. 2b**). It is

6   interesting to point out that the resistance of GP decreased during the bending process,

7   which could be attributed to the compacting effect of 3D GP during bending. **Fig.2c**

8   shows the cyclic bend and release test of GP at a very small bend radius of 1.0 mm. The

9   resistance of GP increases rapidly in the first 10 cycles and becomes stable after 1000

10   cycles (**Fig.2c inset**). There is only 7.3% increase in resistance after 5000 cycles at the

11   tested   small   bend   radius   of   1.0   mm.   These   results   illustrate   the   excellent

12   electromechanical stability of GPs compared with conventional materials used in flexible

13   electronics and other graphene materials such as graphene foam and graphene films [1, 31].

14

15

16   **Table 2**. Electrical conductivity comparison of different graphene scaffolds for EC
17   electrodes.

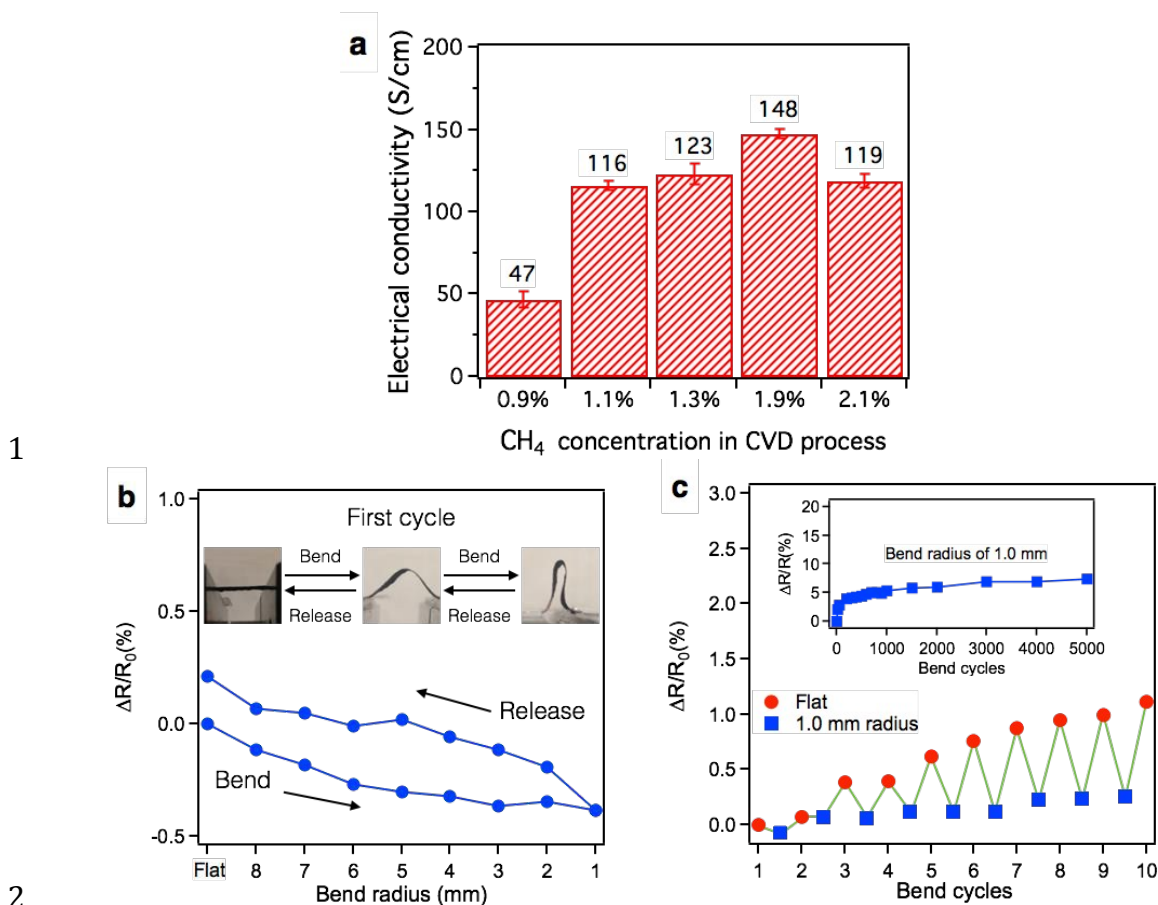| Materials	Electrical conductivity ($S \cdot cm^{-1}$)	Reference
Embossed-chemically modified graphene	12.04	[12]
Reduced graphene oxide	5.65	[29]
Graphene foam	1	[1]
CNT/Graphene foam hybrid film	1.9	[28]
GP	148	This work

18

Figure 2. (a) Electrical conductivity of the GP prepared by using different CH_4 concentrations. The error bars represent the standard deviations that were calculated based on 3 tested specimens for each sample. (b) Variation in electrical resistance of GP as a function of the bend radius up to 1.0 mm and back to flat state during a single bend cycle. The inset shows the bend and release steps. (c) Variation in electrical resistance of a composite during bending in cycles with a radius up to 1.0 mm and then back to flat state. The inset shows the resistance change of GP as a function of the bend cycles for a bend radius of 1.0 mm.

The good electrical and mechanical properties of the 3D graphene pellet make it an

excellent candidate for energy storage applications. To explore this opportunity, we chose

a typical pseudocapacitive material - MnO_2, which allowed us to study the synergistic

effect between GP and this metal oxide. A layer of MnO_2 was electrochemically

deposited on the surface of GP by oxidation of Mn^{2+} to Mn^{4+} in solution, following a

procedure described in the literature[32]. **Figs.3 a-d** show SEM images revealing the

1   morphology of GP after electrochemical coating with MnO_2 with different mass loading.

2   The later was controlled by the time of electro-deposition, which was varied from 5 min

3   to 40 min. Compared to pristine GP (**Fig.3a**), the deposited GP/MnO_2 (11.4 wt% MnO_2)

4   in (**Fig.3b**) showed cluster formation of the coating. These clusters turned into sphere-like

5   structures when the MnO_2 content was increased to 54.5 wt% as shown in **Fig.3c**. The

6   inserted SEM image in **Fig.3c** displays the cross-section of GP/MnO_2 (54.5 wt% MnO_2),

7   where the embedment of MnO_2 spheres into the surface of GP is revealed. This

8   embedment suggests a good contact between MnO_2 and GP, which can be attributed to

9   the unique porous surface morphology of GP. In **Fig.3d** showing the morphology of

10   GP/MnO_2 (79.6 wt% MnO_2) sample, the spheres of metal oxide merged into a bulk layer.

11   The inserted SEM image displays the cross-section view of the coating. Though the

12   thickness of this MnO_2 layer is relatively large compared to other reported work [12, 33], the

13   good electrical properties of GP and the intimately integrated MnO_2 and GP compensate

14   the low electrical conductivity of MnO_2. The calculated areal density of GP/MnO_2

15   composites with 0 wt% 11.4 wt%, 54.5 wt% and 79.6 wt% MnO_2 is 4.5 g/m^2, 5.1 g/m^2,

16   9.9 g/m^2 and 22.3 g/m^2, respectively. This data illustrates the ability of GP to

17   accommodate a high content of MnO_2. The formed MnO_2 thin layer on GP was further

18   investigated by X-ray photoelectron spectroscopy (XPS). As shown in **Fig.3e**, two

19   characteristic peaks of Mn $2p_{1/2}$ and Mn $2p_{3/2}$ at 654.1 and 642.4 eV, respectively, with a

20   binding energy separation of 11.7 eV were observed, which is in a good agreement with

21   previous work [34, 35].

1

2

3
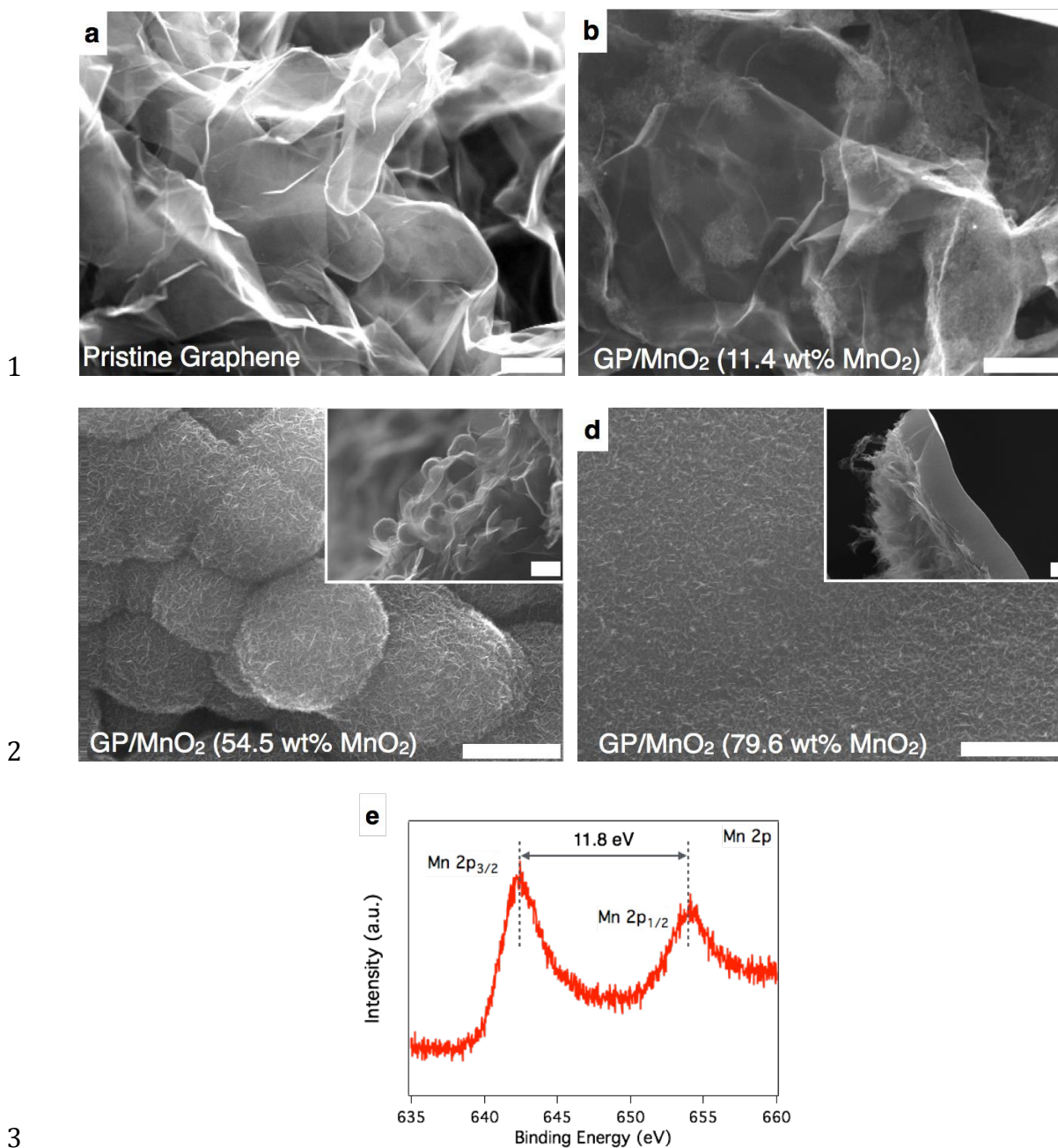
Figure 3. (a) SEM image of pristine GP; (b) SEM image of GP/MnO$_2$ (11.4 wt% MnO$_2$);
(c) SEM images of GP/MnO$_2$ (54.5 wt% MnO$_2$). The inset shows the cross-section view
of this specimen in which the embedment of MnO$_2$ spheres into the surface of GP is
displayed. (d) SEM image of GP/MnO$_2$ (79.6 wt% MnO$_2$). The inset shows the cross-
section view of this specimen in which the formation of a thin MnO$_2$ layer is observed.
All scale bars in the images correspond to 1 μm. (e) Representative Mn 2p XPS spectra of
GP/MnO$_2$ composite.

1　　　　The electrochemical performance of GP and GP/MnO$_2$ composites as capacitive

2　　electrodes were evaluated by a conventional three-electrode system in an aqueous

3　　electrolyte solution of 1 M Na$_2$SO$_4$. As shown in **Fig.4a**, the cyclic voltammetry (CV)

4　　curves of graphene–MnO$_2$ composites reveal no redox peaks due to the surface

5　　adsorption/desorption of protons (H$^+$) or alkaline cations (M$^+$) on the MnO$_2$ surface[36],

6　　indicating that the composites have ideal capacitive behavior. The main capacitance

7　　contributor in the GP/MnO$_2$ composite is expected to be the pseudocapacitance provided

8　　by MnO$_2$, instead of the double-layer capacitance from GP. The latter can be proved by

9　　the fact that during the CV test, increasing the MnO$_2$ mass loading from 11.4 wt% to 79.6

10　　wt% results in a much higher current density compared to pristine GP. We did not study

11　　the electrochemical performance of higher MnO$_2$ mass loading than 79.6 wt% on the GP.

12　　The rational for this came from the obtained CV data suggesting a deviation from the

13　　most favorable rectangular shape at 79.6 wt% MnO$_2$ compared to lower MnO$_2$ content on

14　　the GP. This can be interpreted based on the well-known high resistive behavior of MnO$_2$.

15　　The capacitive performance of GP/MnO$_2$ composite electrodes was further investigated

16　　by the charge-discharge test. For practical applications, both specific capacitance and

17　　volumetric capacitance are critical considering the limited space and load under certain

18　　circumstances. **Fig.4b** shows the increase of both specific and volumetric capacitance of

19　　GP/MnO$_2$ composite electrodes due to the increased mass of MnO$_2$ as revealed by the

20　　SEM images in **Fig.3**. The GP/MnO$_2$ composite electrode shows specific and volumetric

21　　capacitance up to 395 F/g and 230 F/cm^3, which outperforms many other carbon/MnO$_2$

22　　composite electrodes with specific and volumetric capacitance in the order of ~150 F/g

23　　and ~100 F/cm^3, respectively [37-39]. This high value of volumetric capacitance is probably

1   attributed to the more compact structure of GP compared to other reported porous carbon

2   materials such as GF. **Fig.4c** displays the charge-discharge curves of GP/MnO_2 with 79.6

3   wt% MnO_2 mass loading. From the discharging curve there, the specific capacitance of

4   GP/MnO_2 with 79.6 wt% MnO_2 mass loading was calculated to be 395 F/g at 0.8 A/g.

5   These values are higher than those of other reported graphene/MnO_2 materials including

6   GF/MnO_2 composite (240 F/g, 0.1 A/g) [40], MnO_2/graphene composite paper (256 F/g at

7   0.5 A/g) [41], conductive wrapping MnO_2/graphene composite (380 F/g at 0.1 mA/cm^2) [32],

8   and 3D graphene/MnO_2 composite (389 F/g at 1A/g) [12].

9   The synergy of GP as a conducting scaffold for MnO_2 in applications as

10   pseudocapacitive materials is further studied by alternating current impedance

11   measurements at a frequency range from 100 kHz to 0.01 Hz. The obtained results are

12   displayed in **Fig.4d** in the form of Nyquist plots. The pristine GP shows a negligible

13   charge transfer resistance (R_{ct}), which represents the resistance at the interface of the

14   electrode and electrolyte. This result proves an excellent conductivity of GP at the

15   electrode-electrolyte interface. Based on the equivalent series circuit (**Fig.4d inset**) [42, 43],

16   the R_{ct} of the GP/MnO_2 composite electrodes with 54.5 wt% and 79.6 wt% MnO_2 mass

17   loading was calculated. The obtained values were 1.1 Ω and 3.78 Ω, respectively. There

18   is a clear trend showing that the increase of MnO_2 mass loading from 54.5 wt% to 79.6

19   wt% results in rise of R_{ct}, due to the poor electrical conductivity of MnO_2. Still, the R_{ct}

20   values of GP/MnO_2 composite electrodes are relatively small compared to other reported

21   graphene/MnO_2 composite electrodes [28, 32], which supports our assumption that GP can

22   work effectively as good conducting scaffold used in combination with low electrically

23   conductive pseudocapacitive materials such as MnO_2. In the low frequency region, the

18

1   slope of the curve represents the electrolyte and proton diffusion resistance. The pristine

2   GP shows the most ideal straight line along the imaginary axis. A typical Warburg

3   capacitive behavior was observed in which the curve slope decreases with increasing the

4   mass loading of MnO_2, thus indicating higher resistance for ion/proton diffusion.
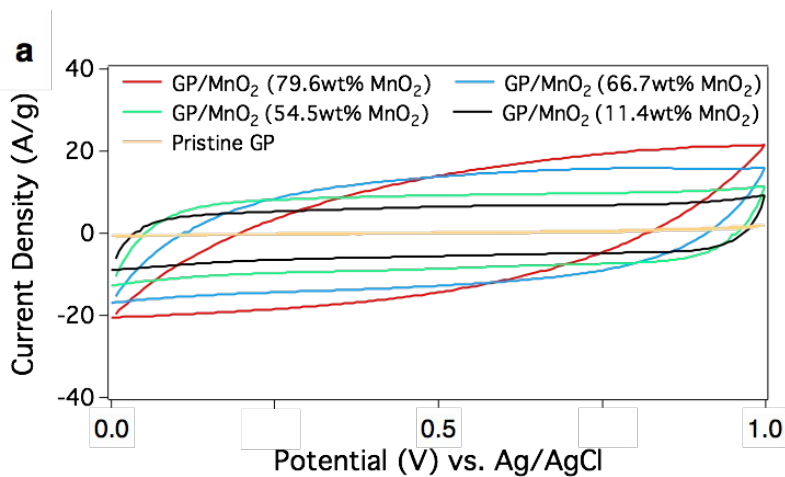
5
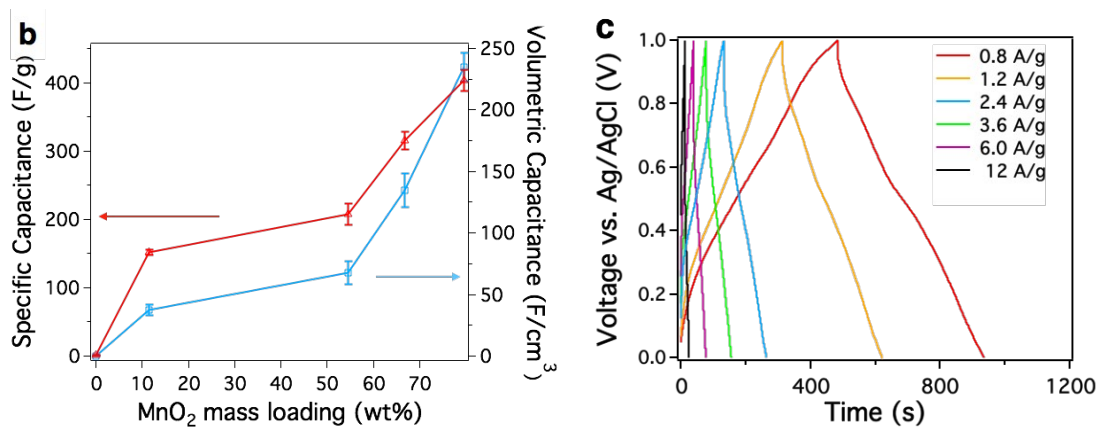
6
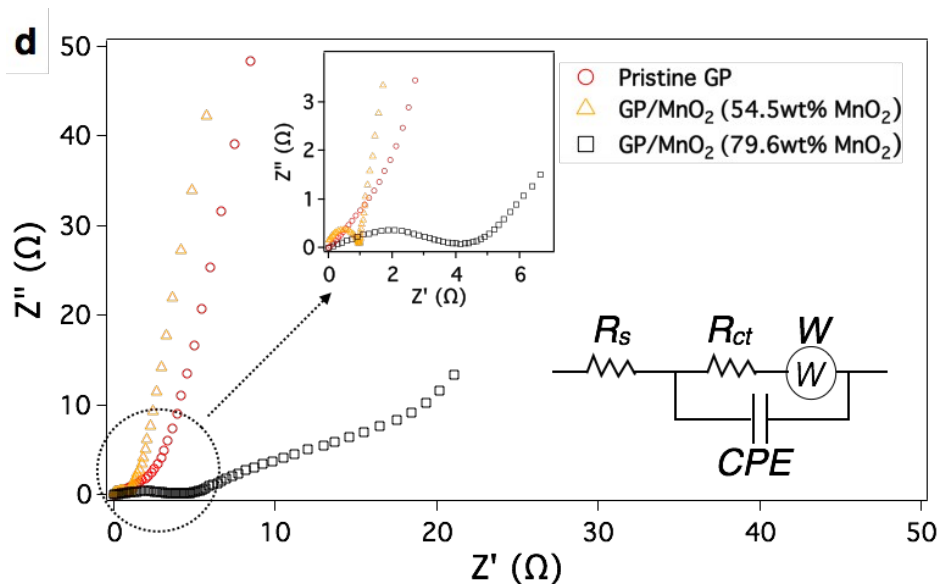
1

2   **Figure 4**. (a) CV curves measured at 50 mV/s for pristine GP and GP/MnO$_2$
3 composites with different MnO$_2$ mass loading from 11.4 wt% to 79.6 wt%; (b) Specific
4 capacitance and volumetric capacitance of GP and GP/MnO$_2$ composites as a function of
5 MnO$_2$ mass loading. Capacitance was estimated from galvanostatic charge-discharge test
6 with a current density of 1 A/g. The error bars represent the standard deviations
7 calculated based on 3 tested specimens for each sample; (c) Galvanostatic charge-
8 discharge curves measured at different current densities from 0.8 to 12 A/g for GP/MnO$_2$
9 composite with 79.6 wt% MnO$_2$ mass loading; (d) Nyquist plots for pristine GP and
10 GP/MnO$_2$ composites with different MnO$_2$ mass loading from 54.5 wt% to 79.6 wt%.
11 The inset shows an equivalent series circuit consisting of electrolyte resistance (R$_s$),
12 interface charge transfer resistance (R$_{ct}$), Warburg element (W) and constant phase
13 element (CPE). All the electrochemical tests were conducted in 1M aqueous solution of
14 Na$_2$SO$_4$ using a three-electrode configuration.

15   We also investigated the electrochemical performance of GP in redox additive

16 electrolyte system that has been studied intensively in recent years due to its ease of

17 preparation and the potential to yield high energy density [44-46]. We believe that the

18 excellent electrical properties of GP can greatly facilitate the chemical reaction of redox

19 additives. **Fig. 5a** shows the CV curves of pristine GP in 1M H$_2$SO$_4$ and 30% acetic acid

20 electrolyte with 50 mM hydroquinone (HQ) and 50 mM benzoquinone (BQ) as redox

21 additives. A high current density in the potential range of 0 - 1.0 V and a couple of redox

22 peaks (HQ to BQ and BQ to HQ) were observed. The charge-discharge curves in **Fig.5b**

1   exhibit an ultrahigh specific capacitance (7813 F/g) of GP at a high current density (10

2   A/g) in HQBQ electrolyte system, which suggests a good synergy of GP with the redox

3   additive electrolyte system. This ultra high specific capacitance comes from the redox

4   reaction between HQ and BQ[45], and GP is proved to efficiently facilitate this process by

5   working as a lightweight and conductive scaffold rather than capacitive material.

6   Interestingly, when the discharge current density was reduced from 20 A/g to 10 A/g, a

7   dramatic increase of specific capacitance was observed. Further decrease of the discharge

8   rate down to 5 A/g will lead to an undesirably long discharging time. This might be

9   attributed to the sufficient diffusion of redox couples into the GP at relatively low current

10   density and needs further studies. After 5000 cycles of charge-discharge at a very high

11   current density of 200 A/g, the specific capacitance dropped by 19.6% (**Fig.5c**) with an

12   increase of R_{ct} after cyclic charge-discharge (CCD) (**Fig.5d**). One plausible reason for the

13   increased R_{ct} is the agglomeration of BQ in the porous graphene structure considering the

14   low solubility of BQ in water [45].

15
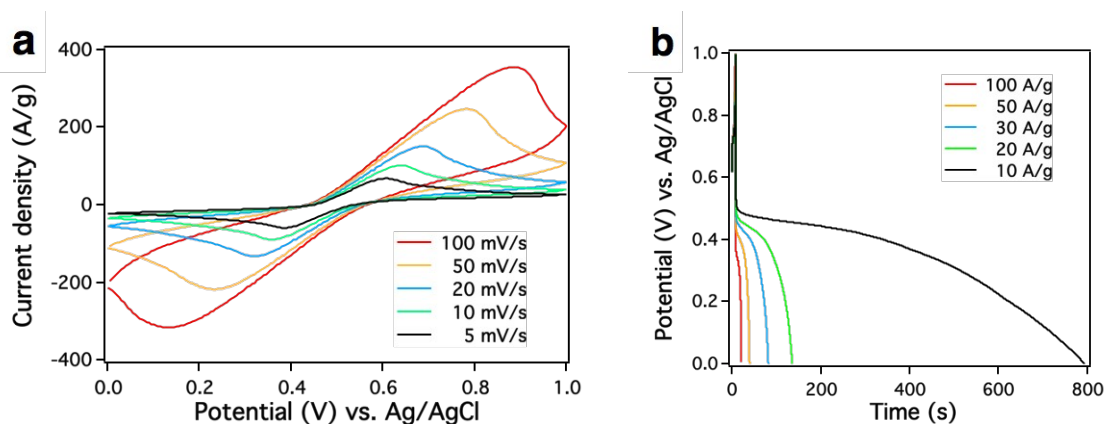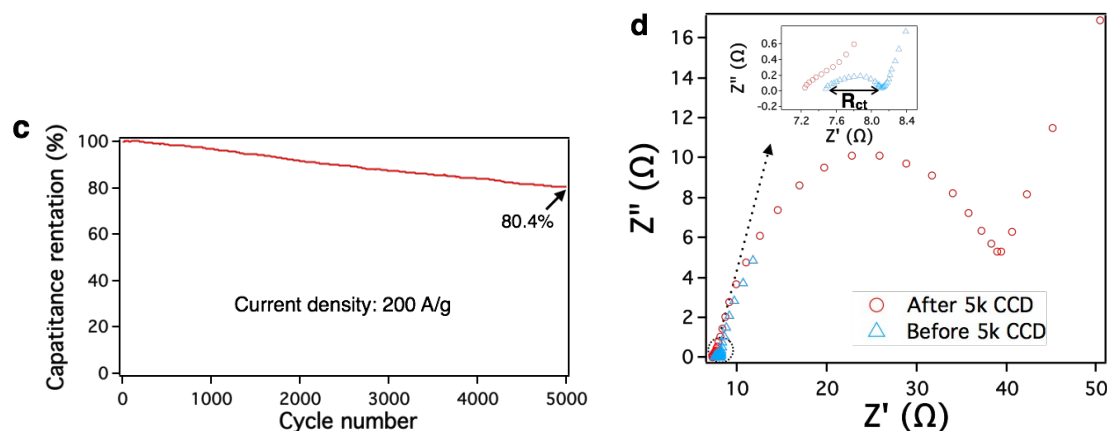
Figure 5. Electrochemical performance of pristine GP in 50mM 1M H_2SO_4 and 30% acetic acid as electrolyte with 50 mM HQ and 50 mM BQ as redox additives. (a) CV curves of GP in HQBQ at different scan rates; (b) Charge-discharge curves of GP in HQBQ at different current density; (c) Capacitance retention curve of GP in HQBQ after 5k CCD. (d) Comparison of GP impedance in HQBQ system before and after 5k CCD.

The full cell performance of asymmetric ECs made of GP/pseudocapacitive materials was also studied. Since the GP/MnO_2 electrode shows a good capacitive performance in the potential range from 0 to 1.0 V, polypyrrole (Ppy) coated GP was employed as a negative electrode to expand the potential range of the asymmetric ECs. This is because Ppy was proven to have a good capacitive performance in the working potential range from -0.6 to 0.2 V [28, 47, 48]. It is also important to balance the charge of the positive and negative electrodes in order to maximize the energy density of ECs. In our work, the electrochemical performance of the GP/Ppy electrode was also investigated (**Fig. S3**). A successful coverage of GP by Ppy was proved by SEM images and Raman spectra displayed in **Fig. S3.** Further, the GP/Ppy electrode shows a specific capacitance of 247 F/g at 1A/g (**Fig.S3c**). The obtained results allowed balancing the mass ratio of the positive electrode (GP/MnO_2) and the negative electrode (GP/Ppy) to 1:2 in order to achieve maximal energy density of ECs. The assembled EC in this work is called GP/MnO_2/Ppy EC. In this system MnO_2 stores energy by adsorption/desorption of

1   protons (H^+) or alkaline cations (Na^+ in our case) on the oxide surface, while Ppy stores

2   energy by doping /de-doping of anions (SO_4^{2-} in our case). In both cases graphene works

3   as a conductive support for those two materials.

4   **Fig.6a** illustrates a schematic structures of the assembled ECs made of an electrolyte

5   (1M Na_2SO_4)-soaked separator sandwiched between positive and negative electrodes.

6   The asymmetric EC shows typical capacitive behavior in the potential range from 0 to 1.6

7   V as displayed in **Fig.6b**. The slow scan rates cause more pronounced rectangular shapes

8   compared to high scan rates. This suggests a more resistive behavior of the device at

9   higher scan rates. There are no redox peaks observed in **Fig.6b**, which is in a good

10   agreement with other reported work[28]. The charge-discharge curves of GP/MnO_2/Ppy EC

11   under different current density are displayed in **Fig.6c**. Based on the IR drop of charge-

12   discharge curves, the GP/MnO_2/Ppy EC exhibits small internal resistances of 24.5 Ω,

13   36.3 Ω, 44.0 Ω and 48.7 Ω at current densities of 10 A/g, 4 A/g, 2 A/g and 1 A/g,

14   respectively. The value of the obtained internal resistance is not as low as we expected

15   considering the good electrical conductivity of GP. A possible explanation is that after

16   the assembly of two different electrodes into a device, the resistance increases because of

17   the differences in the storage mechanisms of these two electrodes. In particular, MnO_2

18   stores energy based on adsorption/desorption of protons (H^+) or via alkaline cations (M^+)

19   on the oxide surface, while Ppy stores energy by doping and de-doping of anions. The

20   different mechanisms result in different charge-discharge speed that contributes to the

21   increased internal resistance of the device. The Nyquist plot in **Fig.6d** reveals a 0.8 Ω

22   electrolyte resistance (R_s) and 24.8 Ω charge transfer resistance $R_{ct,}$ calculated per

23   reference [42], suggesting a fast charge transfer between electrolyte and electrodes. We

1   further calculated the energy density and power density of GP/MnO$_2$/Ppy EC based on

2   charge-discharge curves in **Fig.6c.** The obtained results are presented as a Ragone plot in

3   **Fig.6e**. The GP/MnO$_2$/Ppy EC in our work shows a maximum energy density of 26.7

4   Wh/kg at a power density of 798 W/kg, and a maximum power density (P$_m$) of 16.4

5   kW/kg. The highest P$_m$ was obtained to be 32.7 kW/kg with energy density of 8.9 Wh/kg

6   at a power density of 8.0 kW/kg. Such performance is superior compared to other ECs

7   date reported in the literature [28, 49-51], especially related to a similar GF/MnO$_2$ device

8   showing lower energy density of 8.3 Wh/kg at a power density of 20 kW/kg respectively

9   [40]. The GP/MnO$_2$/Ppy EC also exhibits a good cyclic life with 85% capacitance retention

10   after 5000 cycles charge-discharge at 10 A/g (**Fig.6f**). Furthermore, two stacked

11   GP/MnO$_2$/Ppy ECs were able to power a LED (3.0 V, 30mA) for 1.5 min as shown in

12   **Fig.6g**.

13

1

2
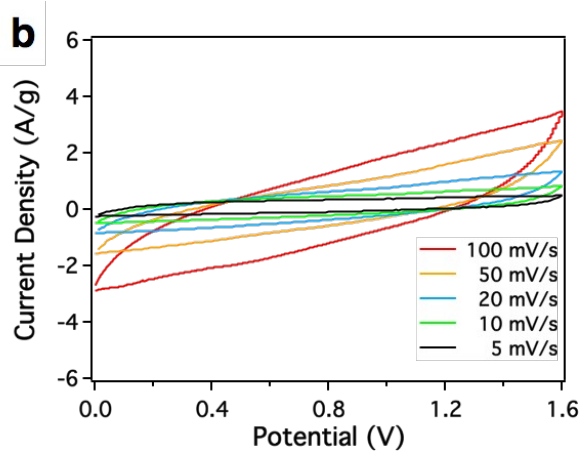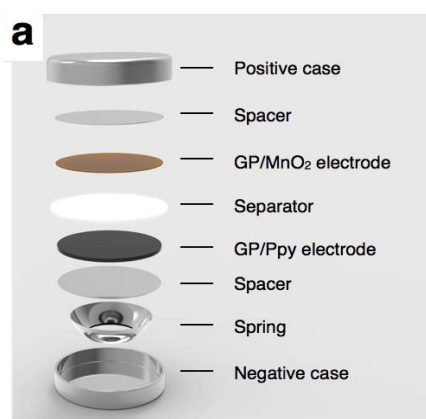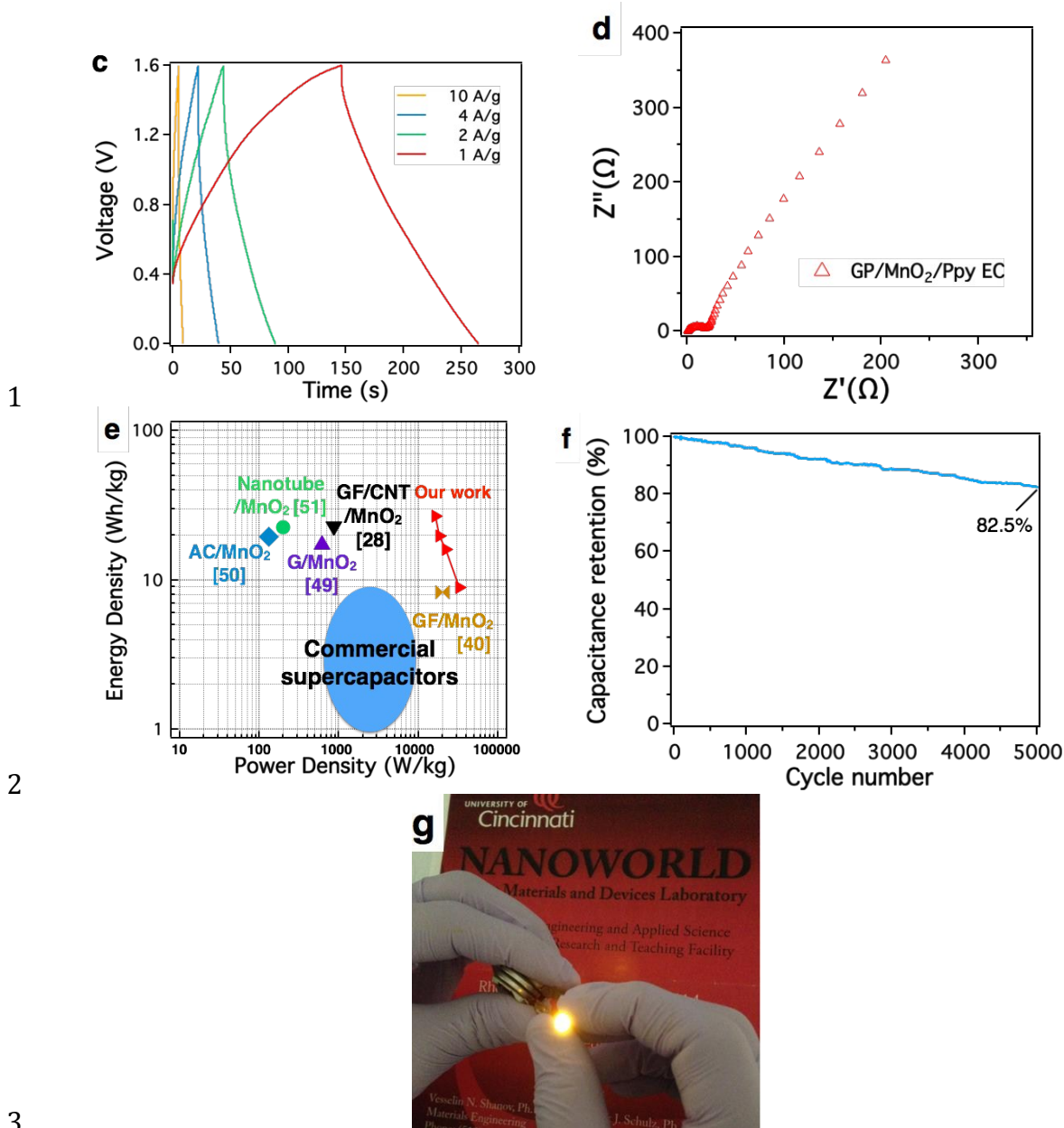
3

4 **Figure 6**. (a) Illustration of GP/MnO$_2$/Ppy EC assembly; (b) CV curves of GP/MnO$_2$/Ppy
5 EC at different scan rates from 5 mV/s to 100 mV/s; (c) Galvanostatic charge-discharge
6 curves measured at different current densities from 1 A/g to 10 A/g for GP/MnO$_2$/Ppy EC;
7 (d) Nyquist plots for GP/MnO$_2$/Ppy EC from 100 kHz to 0.01 Hz; (e) Ragone plot
8 showing data from our GP/MnO$_2$/Ppy EC compared to reference data from other devices
9 that are based on carbon materials performing in aqueous electrolytes, (AC-activated
10 carbon, GF-graphene foam, G-Graphene); (f) CCD test of GP/MnO$_2$/Ppy EC at a constant
11 current density of 10 A/g conducted over 5000 cycles; (g) A two stacked GP/MnO$_2$/Ppy
12 ECs fabricated based on this work powering an LED (3.0 V 30 mA). All the
13 electrochemical tests were conducted in a coin cell device with GP/MnO$_2$ as positive
14 electrode and GP/Ppy as negative electrode separated by an electrolyte (1 M aqueous
15 solution of Na$_2$SO$_4$) soaked separator.

1

2 **Conclusions**

3   We reported a new design and fabrication process of electrode material called

4 graphene pellet (GP) for energy storage applications. The employed catalyst in the form

5 of a sintered nickel template can be easily converted into a GP by CVD. The GPs exhibit

6 good electrical conductivity, electromechanical stability and morphology with a

7 mesoporous structure thus providing great potential for energy storage applications.

8 GP/MnO_2 composites prepared by the described simple electrochemical deposition of

9 MnO_2 onto GP surface showed both high specific and volumetric capacitance with small

10 charge-transfer resistance. This demonstrates good synergy between GP and MnO_2. The

11 excellent electrical and mechanical properties of GP also show great potentials in

12 facilitating chemical reactions typical for redox additive electrolyte systems. Moreover,

13 when the GP/MnO_2 electrode was assembled with GP/Polypyrrole electrode, the obtained

14 full coin cell showed good performance. The simplicity of the 3D graphene preparation

15 allows GP to compete with or replace GF in many energy storage applications.

16 **Acknowledgement**

21
22

23 **References**

24

1.   1.   Z. Chen, W. Ren, L. Gao, B. Liu, S. Pei and H.-M. Cheng, *Nature materials*, 2011,
2.   **10**, 424-428.
3.   2.   X. Yu, B. Lu and Z. Xu, *Advanced Materials*, 2014, **26**, 1044-1051.
4.   3.   X.-C. Dong, H. Xu, X.-W. Wang, Y.-X. Huang, M. B. Chan-Park, H. Zhang, L.-H.
5.   Wang, W. Huang and P. Chen, *ACS Nano*, 2012, **6**, 3206-3213.
6.   4.   Y. He, W. Chen, X. Li, Z. Zhang, J. Fu, C. Zhao and E. Xie, *ACS Nano*, 2013, **7**,
7.   174-182.
8.   5.   X. Dong, X. Wang, J. Wang, H. Song, X. Li, L. Wang, M. B. Chan-Park, C. M. Li and
9.   P. Chen, *Carbon*, 2012, **50**, 4865-4870.
10.   6.   C. Zhao, W. Zheng, X. Wang, H. Zhang, X. Cui and H. Wang, *Scientific Reports*,
11.   2013, **3**, 2986.
12.   7.   X. Cao, Y. Shi, W. Shi, G. Lu, X. Huang, Q. Yan, Q. Zhang and H. Zhang, *Small*,
13.   2011, **7**, 3163-3168.
14.   8.   J. Luo, J. Liu, Z. Zeng, C. F. Ng, L. Ma, H. Zhang, J. Lin, Z. Shen and H. J. Fan, *Nano*
15.   *Letters*, 2013, **13**, 6136-6143.
16.   9.   N. Li, Z. Chen, W. Ren, F. Li and H.-M. Cheng, *Proceedings of the National*
17.   *Academy of Sciences*, 2012, **109**, 17360-17365.
18.   10.   G. Zhou, L. Li, C. Ma, S. Wang, Y. Shi, N. Koratkar, W. Ren, F. Li and H.-M. Cheng,
19.   *Nano Energy*, 2015, **11**, 356-365.
20.   11.   W. Zhang, J. Zhu, H. Ang, Y. Zeng, N. Xiao, Y. Gao, W. Liu, H. H. Hng and Q. Yan,
21.   *Nanoscale*, 2013, **5**, 9651-9658.
22.   12.   B. G. Choi, M. Yang, W. H. Hong, J. W. Choi and Y. S. Huh, *ACS Nano*, 2012, **6**,
23.   4020-4028.
24.   13.   S. Chen, J. Zhu, X. Wu, Q. Han and X. Wang, *ACS nano*, 2010, **4**, 2822-2830.
25.   14.   K. Zhang, L. Mao, L. L. Zhang, H. S. O. Chan, X. S. Zhao and J. Wu, *Journal of*
26.   *Materials Chemistry*, 2011, **21**, 7302-7307.
27.   15.   F. Liu, S. Song, D. Xue and H. Zhang, *Advanced Materials*, 2012, **24**, 1089-1094.
28.   16.   Z. Wen, X. Wang, S. Mao, Z. Bo, H. Kim, S. Cui, G. Lu, X. Feng and J. Chen,
29.   *Advanced Materials*, 2012, **24**, 5610-5616.
30.   17.   Y. Xu, K. Sheng, C. Li and G. Shi, *ACS Nano*, 2010, **4**, 4324-4330.
31.   18.   J. H. Lee, N. Park, B. G. Kim, D. S. Jung, K. Im, J. Hur and J. W. Choi, *ACS Nano*,
32.   2013, **7**, 9366-9374.
33.   19.   L. Zhang, N. T. Alvarez, M. Zhang, M. Haase, R. Malik, D. Mast and V. Shanov,
34.   *Carbon*, 2015, **82**, 353-359.
35.   20.   W. Li, S. Gao, L. Wu, S. Qiu, Y. Guo, X. Geng, M. Chen, S. Liao, C. Zhu, Y. Gong, M.
36.   Long, J. Xu, X. Wei, M. Sun and L. Liu, *Scientific Reports*, 2013, **3**, 2125.
37.   21.   C. Shan, H. Tang, T. Wong, L. He and S.-T. Lee, *Advanced Materials*, 2012, **24**,
38.   2491-2495.
39.   22.   Z. Chen, W. Ren, B. Liu, L. Gao, S. Pei, Z.-S. Wu, J. Zhao and H.-M. Cheng, *Carbon*,
40.   2010, **48**, 3543-3550.
41.   23.   D. Yu, K. Goh, H. Wang, L. Wei, W. Jiang, Q. Zhang, L. Dai and Y. Chen, *Nat Nano*,
42.   2014, **9**, 555-562.
43.   24.   X. Wang, Y. Zhang, C. Zhi, X. Wang, D. Tang, Y. Xu, Q. Weng, X. Jiang, M. Mitome,
44.   D. Golberg and Y. Bando, *Nat Commun*, 2013, **4**.
45.   25.   K. Jurewicz, E. Frackowiak and F. Béguin, *Appl. Phys. A*, 2004, **78**, 981-987.

26. C. Vix-Guterl, E. Frackowiak, K. Jurewicz, M. Friebe, J. Parmentier and F. Béguin, *Carbon*, 2005, **43**, 1293-1302.

27. F. Béguin, M. Friebe, K. Jurewicz, C. Vix-Guterl, J. Dentzer and E. Frackowiak, *Carbon*, 2006, **44**, 2392-2398.

28. J. Liu, L. Zhang, H. B. Wu, J. Lin, Z. Shen and X. W. Lou, *Energy & Environmental Science*, 2014, **7**, 3709-3719.

29. A. Sumboja, C. Y. Foo, X. Wang and P. S. Lee, *Advanced Materials*, 2013, **25**, 2809-2815.

30. J. A. Rogers, T. Someya and Y. Huang, *Science*, 2010, **327**, 1603-1607.

31. K. S. Kim, Y. Zhao, H. Jang, S. Y. Lee, J. M. Kim, K. S. Kim, J.-H. Ahn, P. Kim, J.-Y. Choi and B. H. Hong, *Nature*, 2009, **457**, 706-710.

32. G. Yu, L. Hu, N. Liu, H. Wang, M. Vosgueritchian, Y. Yang, Y. Cui and Z. Bao, *Nano Letters*, 2011, **11**, 4438-4442.

33. S. W. Lee, J. Kim, S. Chen, P. T. Hammond and Y. Shao-Horn, *Acs Nano*, 2010, **4**, 3889-3896.

34. M. Toupin, T. Brousse and D. Bélanger, *Chemistry of Materials*, 2004, **16**, 3184-3190.

35. A. L. M. Reddy, M. M. Shaijumon, S. R. Gowda and P. M. Ajayan, *Nano Letters*, 2009, **9**, 1002-1006.

36. Q. Qu, P. Zhang, B. Wang, Y. Chen, S. Tian, Y. Wu and R. Holze, *The Journal of Physical Chemistry C*, 2009, **113**, 14020-14027.

37. J. R. Miller and A. F. Burke, *The Electrochemical Society Interface*, 2008, **17**, 53.

38. P. Simon and A. F. Burke, *The electrochemical society interface*, 2008, **17**, 38.

39. Y. J. Kim, Y. Abe, T. Yanagiura, K. C. Park, M. Shimizu, T. Iwazaki, S. Nakagawa, M. Endo and M. S. Dresselhaus, *Carbon*, 2007, **45**, 2116-2125.

40. A. Bello, O. O. Fashedemi, J. N. Lekitima, M. Fabiane, D. Dodoo-Arhin, K. I. Ozoemena, Y. Gogotsi, A. T. Charlie Johnson and N. Manyala, *AIP Advances*, 2013, **3**, 082118.

41. Z. Li, Y. Mi, X. Liu, S. Liu, S. Yang and J. Wang, *Journal of Materials Chemistry*, 2011, **21**, 14706-14711.

42. B. G. Choi, J. Hong, W. H. Hong, P. T. Hammond and H. Park, *ACS Nano*, 2011, **5**, 7205-7213.

43. M. V. Reddy, T. Yu, C. H. Sow, Z. X. Shen, C. T. Lim, G. V. Subba Rao and B. V. R. Chowdari, *Advanced Functional Materials*, 2007, **17**, 2792-2799.

44. G. Ma, M. Dong, K. Sun, E. Feng, H. Peng and Z. Lei, *Journal of Materials Chemistry A*, 2015, **3**, 4035-4041.

45. D. Vonlanthen, P. Lazarev, K. A. See, F. Wudl and A. J. Heeger, *Advanced Materials*, 2014, **26**, 5095-5100.

46. S.-E. Chun, B. Evanko, X. Wang, D. Vonlanthen, X. Ji, G. D. Stucky and S. W. Boettcher, *Nat Commun*, 2015, **6**.

47. C. Xu, J. Sun and L. Gao, *Journal of Materials Chemistry*, 2011, **21**, 11253-11258.

48. Y. Zhao, J. Liu, Y. Hu, H. Cheng, C. Hu, C. Jiang, L. Jiang, A. Cao and L. Qu, *Advanced Materials*, 2013, **25**, 591-595.

49. T. Cottineau, M. Toupin, T. Delahaye, T. Brousse and D. Bélanger, *Appl. Phys. A*, 2006, **82**, 599-606.

Journal of Materials Chemistry A Accepted Manuscript

1   50.   Q. T. Qu, Y. Shi, S. Tian, Y. H. Chen, Y. P. Wu and R. Holze, *Journal of Power*
2   *Sources*, 2009, **194**, 1222-1225.
3   51.   M. Huang, Y. Zhang, F. Li, L. Zhang, R. S. Ruoff, Z. Wen and Q. Liu, *Scientific*
4   *Reports*, 2014, **4**, 3878.
5
6